Supplementary Information

Benefits and Yields of Simultaneous HClO and H_2 Generation in Side-Emitting Optical Fiber Photocatalytic Reactors

Han Fu, Ethan Sheard, Jirapat Ananpattarachai, Daisuke Ioka, Zhenhua Pan, Paul Westerhoff

[1] School of Sustainable Engineering and the Built Environment, Ira A. Fulton Schools of Engineering, Arizona State University, Tempe, AZ 85287-3005, USA

[2] Department of Applied Chemistry, Graduate School of Engineering, University of Hyogo, Himeji, Hyogo 671-2280, Japan

*Corresponding author: Paul Westerhoff

Email: p.westerhoff@asu.edu

Section S1. Synthesis of RhCrCoOx-deposited SrTiO3:Al (STO)

Based on the previous studies [1, 2], Al-doped strontium titanate ($SrTiO_3$:Al) was synthesized using a $SrCl_2$ flux-assisted solid-state method following a previously reported procedure. $SrCl_2$ (Kanto Chemicals Co., Inc., 98.0%, anhydrous), Al_2O_3 nanopowder (Sigma-Aldrich), and $SrTiO_3$ powder (Wako Pure Chemicals Industries, Ltd., 99.9%) were mixed at a molar ratio of 10:0.02:1 and homogenized by grinding in an agate mortar. The mixture was transferred to an alumina crucible and annealed at 1423 K for 10 h in air, followed by natural cooling to room temperature. After calcination, the solid product was repeatedly washed with distilled water to remove residual $SrCl_2$. Washing and filtration continued until the supernatant reached neutral pH. The recovered $SrTiO_3$:Al powder was then dried in an oven at 313 K.

$RhCrCoO_x$ cocatalysts were deposited onto $SrTiO_3$:Al by an impregnation method using aqueous precursor solutions. $RhCl_3 \cdot 6H_2O$ (Wako Pure Chemical Industries), K_2CrO_4 (Kanto Chemical Co.), and $Co(NO_3)_2 \cdot 6H_2O$ (Kanto Chemical Co.) were used as Rh, Cr, and Co sources, respectively. For each batch, 0.4 g of $SrTiO_3$:Al was dispersed in 2 mL of distilled water under sonication and magnetic stirring. Freshly prepared precursor solutions were then added to achieve nominal loadings of 0.1 wt% each of Rh, Cr, and Co relative to the mass of $SrTiO_3$:Al. The suspension was stirred and evaporated to dryness in a water bath. The resulting powder was collected and calcined in air at 350 °C for 1 h with a heating rate of 10 °C min^{-1} to obtain $RhCrCoO_x/SrTiO_3$:Al.

Section S2. Fabrication and characterization of POF-STO

POF-STO samples were fabricated following the procedure illustrated in **Figure S1**, based on our previous studies [2]. Commercial polymer optical fibers (POFs, 3 mm diameter) consisting

of a PMMA core and fluorinated polymer cladding were obtained from Industrial Fiber Optics Inc. (Model Eaka™ CK-120). Fibers were cut into 16 cm lengths and cleaned with isopropanol (>99%, Sigma-Aldrich) prior to surface treatment.

In Step 1, POF surface etching was conducted to enhance side-emission and increase surface roughness for STO deposition. Cleaned POFs were immersed in dimethylformamide (99.8%, Sigma-Aldrich) for 2 s, immediately withdrawn, and dried at room temperature. This etching cycle was repeated four times. In Step 2, both ends of each etched POF were polished sequentially using five grades of optical polishing paper (LE30D, LE5P, LE3P, LE1P, and LE03P, Thorlabs™) until a smooth, mirror-like finish was achieved.

In Step 3, an STO suspension was prepared by dispersing STO powder, colloidal silica binder (Nissan Chemical Inc., ST-OUP), and calcium chloride (VWR, Catalog No. 0556) in 50 mL of ethanol (Pure 200 proof, anhydrous, ⩾99.5, Sigma-Aldrich) at a mass ratio of 4.0:1.0:0.046. The STO concentration was fixed at 5 mg mL^{-1}. The suspension was sonicated in a water bath sonicator (Branson M5800) for 30 min to ensure homogeneous dispersion (Step 4).

In Step 5, spray coating was performed by vertically mounting five etched and polished POFs on a rotating platform. A drying fan positioned to the right of the platform maintained a local temperature of 65–70 °C. The STO suspension was sprayed from the left side using a manual airbrush sprayer (Gocheer™ Airbrush Kit, Model 101-BMC). The total sprayed volume was varied between 10 and 50 mL to control catalyst loading. In Step 6, the coated fibers were dried at 90 °C for 4 h. After drying, the POF-STO samples were rinsed with isopropanol to remove loosely attached STO particles and dried again at 60 °C for 1 h prior to use.

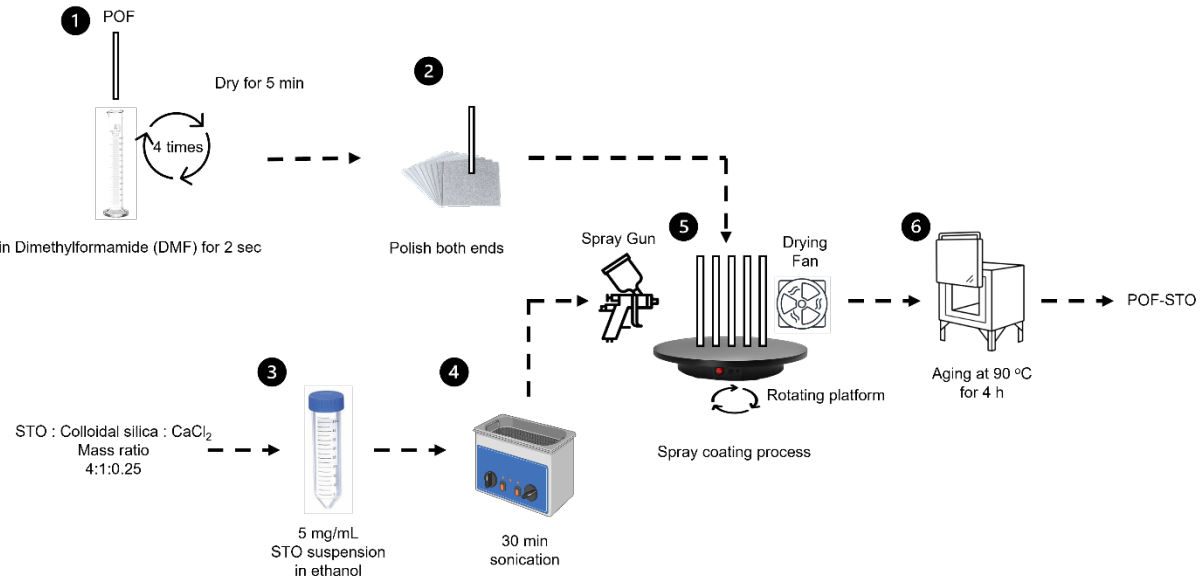

Figure S1. Synthesis pathway of POF-STO

Section 3 Estimation of the total side-emitted power (*P*s)

Optical properties were evaluated by measuring photon irradiance, including the total light input at the proximal end (I_0), side-emitted light intensity (I_S) per 0.4 cm fiber length, and transmitted light intensity at the distal end (I_T). Light irradiance (μW cm^{-2}) was measured using a spectroradiometer (Avantes AvaSpec-2048 L), as shown in **Figure S2a**. Furthermore, **Figure S2b** shows the total light input (I_0, μW cm^{-2}) at the proximal end of the fiber entering the POF can be represented according to the following formula [2-4]:

$$I_0 = I_{Abs}+I_S+I_U+I_T \quad \text{(S1)}$$

where I_{Abs} is light irradiance absorbed by bare POF materials, I_S is the side-emitted light, I_U is the light irradiance absorbed and utilized by the STO within the POF cladding, and I_T is the transmitted light irradiance from the distal end of the POF.

The total side-emitted power (*P*s) was calculated by integrating the local side-emission irradiance ($I_{s,x}$) measured at 0.4 cm intervals along the active fiber length (L = 16 cm). As detailed in the calculation model (**Figure S2c**), the integration is defined as [3, 4]:

$$P_s\,(\mu W) = I_S\ (\mu W\ cm^{-2}) \times \text{lateral surface area } (cm^2) = 2\,\pi r \times \int_{x=0}^{x=16\ cm} I_{s,x}\,dx \quad \text{(S2)}$$

where r is the fiber radius (0.15 cm) and $I_{s,x}$ is the measured local irradiance at position x (each 0.45 cm). The reactor was operated using a UV-LED source driven at three distinct electrical power levels: 3 W, 5 W, and 10 W. By applying Equation S2 to the measured irradiance profiles, the effective *P*s values were determined to be **0.27 W, 0.45 W, and 0.90 W**, respectively.

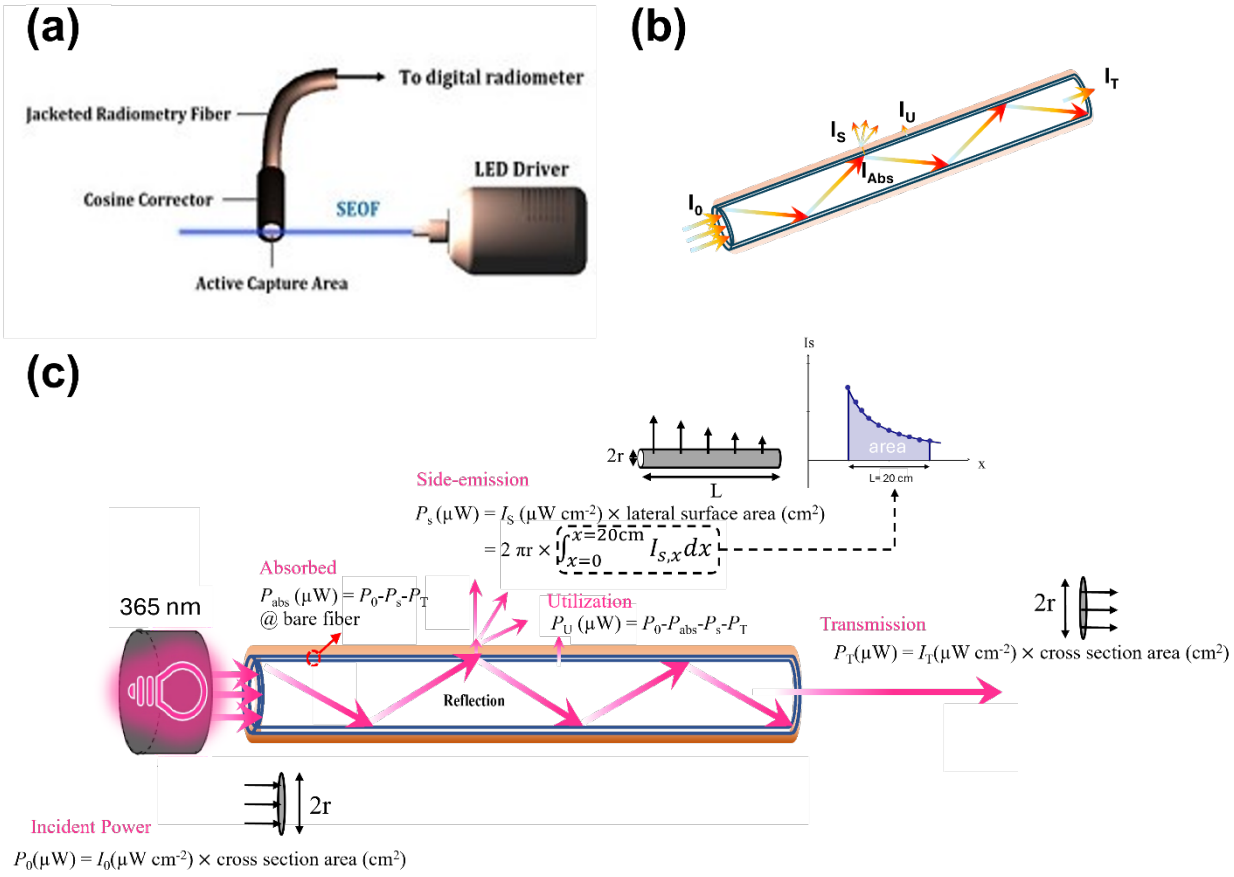

Figure S2. Schematic of the optical characterization setup and photon energy balance analysis. (a) Experimental setup showing the spectroradiometer coupled to a cosine corrector for measuring local irradiance. (b) Conceptual illustration of light propagation modes within the POF-STO composite, identifying input (I_0), side-emission (I_s), utilization (I_U), and transmission (I_T). (c) Detailed photon power balance model defining the calculation of Side-Emitted Power (P_s) via Equation S2, integrating the measured irradiance over the lateral surface area of the fiber.

Section S4. Calculation of Stoichiometric Charge Balance

To verify that the fundamental principle of charge neutrality is strictly maintained during the simultaneous co-generation process, the stoichiometric balance between photogenerated electrons (e^-) and holes (h^+) was quantified for all experimental trials. The overall photocatalytic process relies on one reduction half-reaction and two competing oxidation half-reactions. The reduction of protons to drive H_2 evolution consumes two electrons per molecule of H_2 generated. Concurrently, the photogenerated holes are consumed by two parallel pathways: the selective oxidation of chloride to produce HClO, which requires two holes per molecule, and the competing oxidation of water to evolve O_2, which requires four holes per molecule.

$$2 \times R_{H_2}(electrons) = 2 \times R_{HClO}(holes) + 4 \times R_{O_2}(holes) \qquad \text{(S3)}$$

To evaluate the macroscopic charge neutrality of the system, the total molar consumption rate of holes was compared directly against the total molar consumption rate of electrons. The measured generation rates of the three primary products H_2, HClO, and O_2, were utilized to calculate this ratio. To ensure unit consistency, the measured aqueous free chlorine generation rate was first converted into a molar rate μmol h^{-1}, using the established reactor volume. The experimental charge balance percentage was subsequently calculated using the following equation:

$$Charge\ Balance\ (\%) = \frac{2 \times n(HClO) + 4 \times n(O_2)}{2 \times n(H_2)} \times 100 \qquad \text{(S4)}$$

In this equation, *n* represents the measured molar generation rate of each respective product. An ideal closed system exhibiting perfect charge utilization without intermediate radical accumulation should yield a charge balance of exactly 100%. The calculated average experimental charge balance of 97.2% across the design space quantitatively confirms that global charge neutrality is fundamentally preserved by the complementary water oxidation reaction, even under operational regimes where the targeted HClO generation rate is mass-transport limited. The detailed

experimental measurements and the resulting charge balance for each of the fifteen design space trials are provided in Table S1 below.

Table S1. Experimental Data and Charge Balance Deviation across RSM Trials

Run	Free Chlorine Rate (μmol h^{-1})	H_2 Evolution Rate (μmol h^{-1})	O_2 Evolution Rate (μmol h^{-1})	Charge Balance (%)
1	0.03	42.78	20.31	95.00%
2	0.08	67.22	31.56	94.00%
3	0.25	64.27	29.45	92.00%
4	0.96	50.95	24.25	97.10%
5	0.14	63.84	31.53	99.00%
6	0.79	45.69	22.90	102.00%
7	0.75	64.47	31.03	97.40%
8	0.77	55.68	26.20	95.50%
9	0.62	61.79	30.19	98.70%
10	0.01	61.03	31.55	103.40%
11	0.09	63.04	30.98	98.40%
12	0.14	49.73	23.68	95.50%
13	0.96	52.62	24.98	96.80%
14	0.00	67.67	31.67	93.60%
15	0.50	50.48	24.84	99.40%

Section S5 Apparent Quantum Yield (AQY) Calculation

The Apparent Quantum Yield (AQY) for hydrogen evolution was calculated based on the effective side-emitted photon flux utilizing the following equation:

$$AQY(\%) = \frac{2 \times Number\ of\ evolved\ H_2\ molecules}{Number\ of\ incident\ photons} \times 100 \quad \text{(S5)}$$

To determine the incident photon flux (number of photons per second), the total side-emitted optical power (P_s, measured in J/s or Watts) was divided by the energy of a single photon (E_p). The energy of a single photon at the excitation wavelength (λ) was calculated using the Planck-Einstein relation:

$$E_p = \frac{hc}{\lambda} \quad \text{(S6)}$$

where h is Planck's constant, c is the speed of light in a vacuum, and λ is the excitation wavelength. Therefore, the total incident photon flux can be expressed as:

$$Incident\ photon\ flux = \frac{p_s \times \lambda}{hc} \quad \text{(S7)}$$

Using the measured side-emitted power inputs (**0.27 W, 0.45 W, and 0.90 W**), the total photon flux was determined and applied to the AQY equation. The calculated AQY for all 15 experimental runs is summarized in Table S2.

Section S6. Turnover Frequency (TOF) Calculation

The Turnover Frequency (TOF) evaluates the intrinsic catalytic activity of the loaded cocatalysts by normalizing the product generation rate against the exact number of available active metal sites. In this POF-STO system, the RhCrCoOx cocatalyst features a distinct structural mechanism. The Rhodium (Rh) core serves as the primary active site for the reduction half-reaction (H_2 evolution). The Chromium Oxide (CrO_x) forms a selectively permeable protective shell and does not act as the primary catalytic center. Instead, the Cobalt Oxyhydroxide (CoOOH) layer acts as the active

hole scavenger, driving the oxidation half-reaction (HClO generation and competitive OER) while protecting the structure from oxidative corrosion.

Consequently, the TOF for H_2 evolution was normalized against the available Rhodium sites, while the TOF for HClO generation was normalized against the available Cobalt sites. Assuming a 0.1 wt% loading for both active metals, the moles of active Rh sites (n_{Rh}) and Co sites (n_{Co}) were calculated using their respective atomic weights (M_{Rh} = 102.9 g mol^{-1}, M_{Co} = 58.93 g mol^{-1}) and the total mass of the loaded STO catalyst;

$$n_{Rh} = \frac{m_{STO} \times 0.001}{102.9} \quad \text{(S8)}$$

$$n_{Co} = \frac{m_{STO} \times 0.001}{58.93} \quad \text{(S9)}$$

The TOF (expressed in h^{-1}) for the target reduction and oxidation reactions was then calculated by dividing the experimental molar generation rate of each product by the moles of its corresponding active metal site:

$$TOF_{H_2} = \frac{n(H_2)}{n_{Rh}} \quad \text{(S10)}$$

$$TOF_{HClO} = \frac{n(HClO)}{n_{Co}} \quad \text{(S11)}$$

These site-specific calculations allow for the direct evaluation of the kinetic efficiency of the individual reduction and oxidation half-reactions based on their true mechanistic active sites, independently of the total catalyst mass. All the calculated values were summarized in **Table S2**.

Table S2 Estimated Apparent Quantum Yield (AQY) and Turnover Frequency (TOF) for the 15-run experimental matrix.

Run	Normalized H_2 Rate (mmol g^{-1} h^{-1})	Normalized HClO Rate (mmol g^{-1} h^{-1})	AQY H_2 (%)	TOF H_2 (h^{-1})	TOF HClO (h^{-1})
1	13.44	0.00	1.73	587.00	0.20
2	6.43	0.02	4.54	2770.80	1.60
3	3.40	0.03	1.30	1322.80	2.60
4	12.77	0.06	3.44	699.20	6.70
5	3.05	0.03	1.29	2631.70	2.90
6	12.89	0.05	1.85	627.00	5.50
7	5.57	0.15	4.35	2657.70	15.50
8	6.18	0.08	2.25	1145.90	8.00
9	6.10	0.06	1.25	1271.80	6.50
10	12.61	0.00	4.12	1256.00	0.10
11	3.32	0.02	2.55	2598.70	1.90
12	3.51	0.01	3.36	682.40	1.00
13	13.53	0.06	1.07	722.10	6.60
14	3.37	0.00	1.37	2789.40	0.00
15	2.85	0.03	1.02	692.70	3.40

Table S3 Benchmark comparison of the POF-STO architecture against state-of-the-art photocatalytic systems in saline water [5-10].

Photocatalyst System	Reaction Medium	Light Source	H_2 Yield (mmol g^{-1} h^{-1})	HClO / Cl_2 Yield	AQY (%)	H_2 TOF (h^{-1})
POF-STO (This Work)	H_2 & HClO Co-Generation	365 nm LED	13.5	150 umol g^{-1} h^{-1}	4.54 at 365 nm	587-2789
Ir/TiO_2 Heterojunction	Seawater	Full-spectrum light	9.8- 46.0	Not reported	86.5 at 365 nm	1163
H-TiO_2/Cu_2O	Natural Seawater	365 nm light	17.9 to 45.7	Not reported	14.9 to 18.8 at 365 nm	-
1 wt% Pt/TiO_2	0.5 M NaCl Brine	365 nm LED	-	70 umol h^{-1} (Cl_2)	4.3 at 365 nm	-
BiOCl-N-OV	CO_2-saturated NaCl	Visible light (300 W Xe, >400 nm)	CO evolved	87.2 umol g^{-1} h^{-1}	0.69 at 400 nm	-

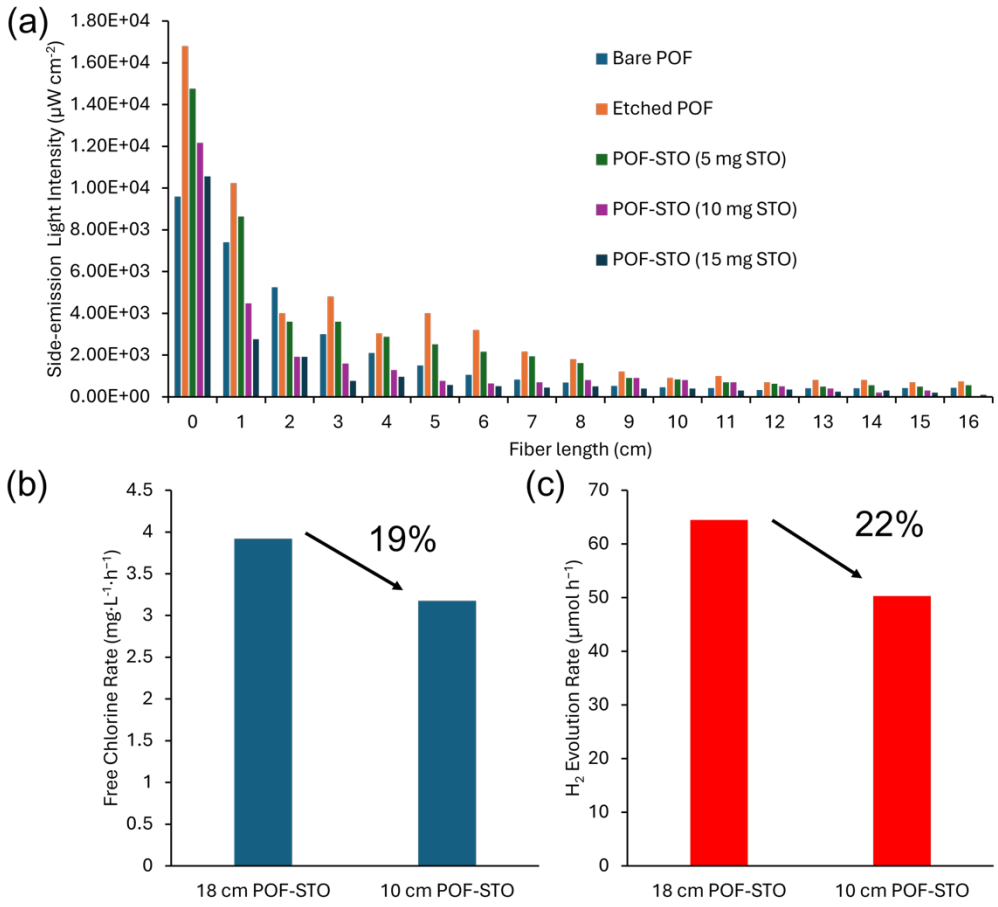

208

209 **Figure S3.** Side-emitting light intensity of the POF-STO. (a) Side-emission intensity along bare,

210 etched, and STO-coated fibers. (b) Free chlorine and (c) H_2 evolution rates comparing 18 cm and

211 10 cm POF-STO reactors, demonstrating that most catalytic activity occurs within the first 10 cm.

212

213

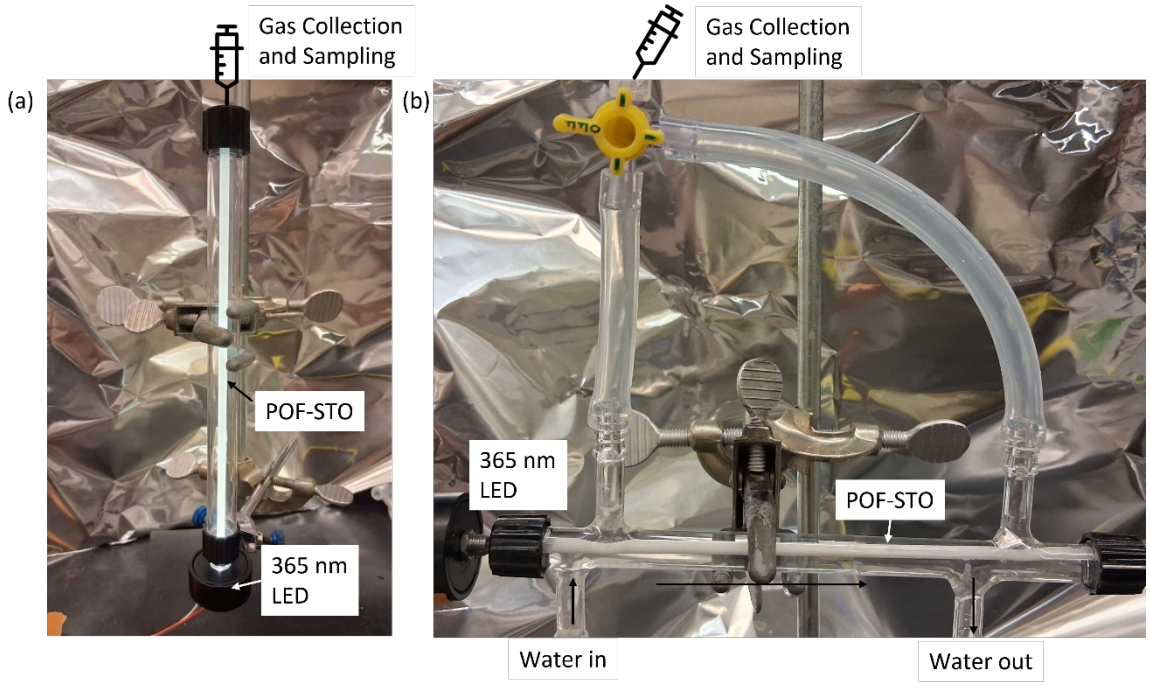

214

215 **Figure S4.** the real reactor setup for a) Batch system for RSM optimization, Mode 1 (Shock

216 Disinfection), and Mode 3 (Fuel-Priority). (b) continuous flow system for Mode 2 (Maintenance

217 Mode).

218

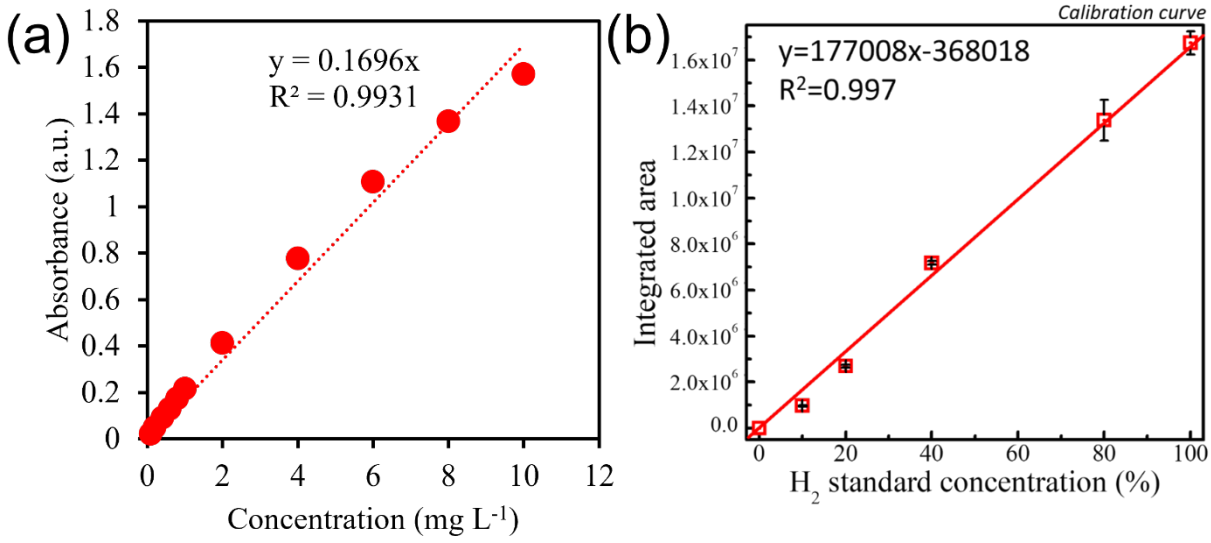

219

220 **Figure S5**. Standard calibration curves for quantitative analysis. (a) Calibration plot for aqueous

221 free chlorine (HClO) concentration. (b) Calibration plot for hydrogen (H_2) gas.

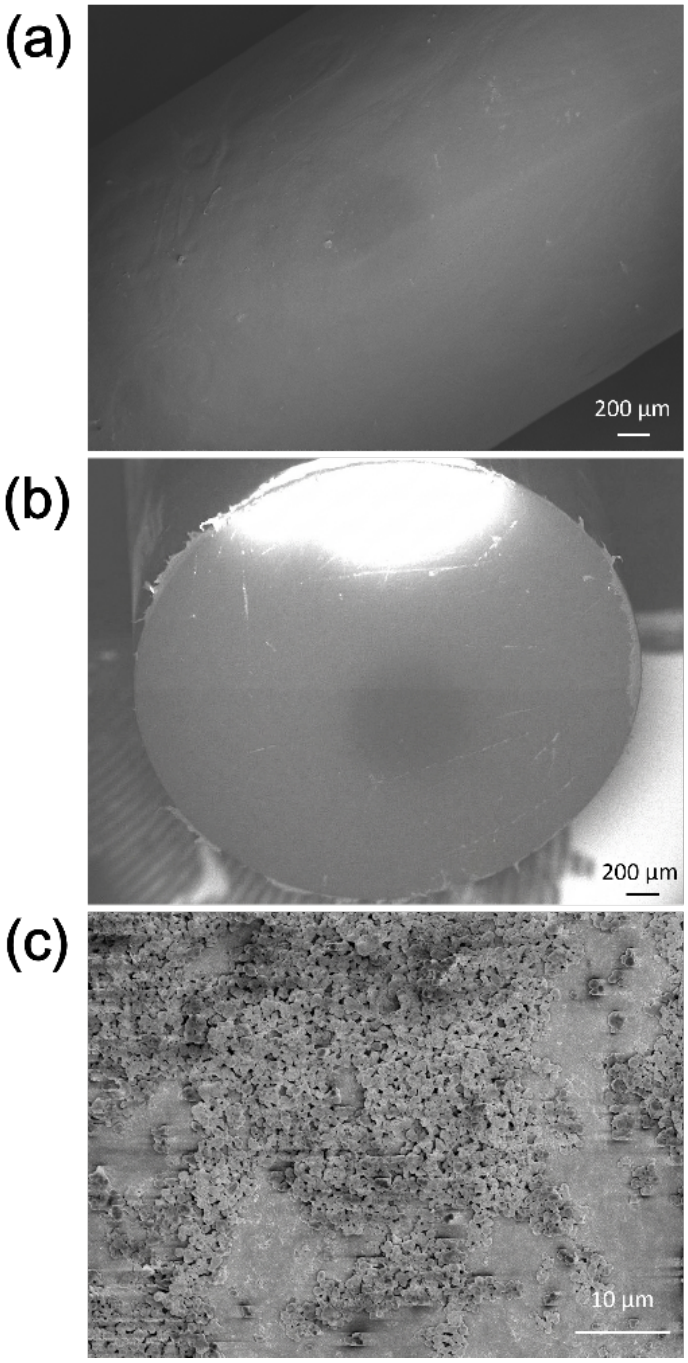

Figure S6 Characterization of the POF-STO (10 mg STO loading). (a) Low-magnification lateral surface of the POF-STO. (b) Cross-section of the POF-STO. (c) High-magnification morphology of the deposited STO catalyst layer. The SEM images was taken using a Zeiss Auriga FIB-SEM.

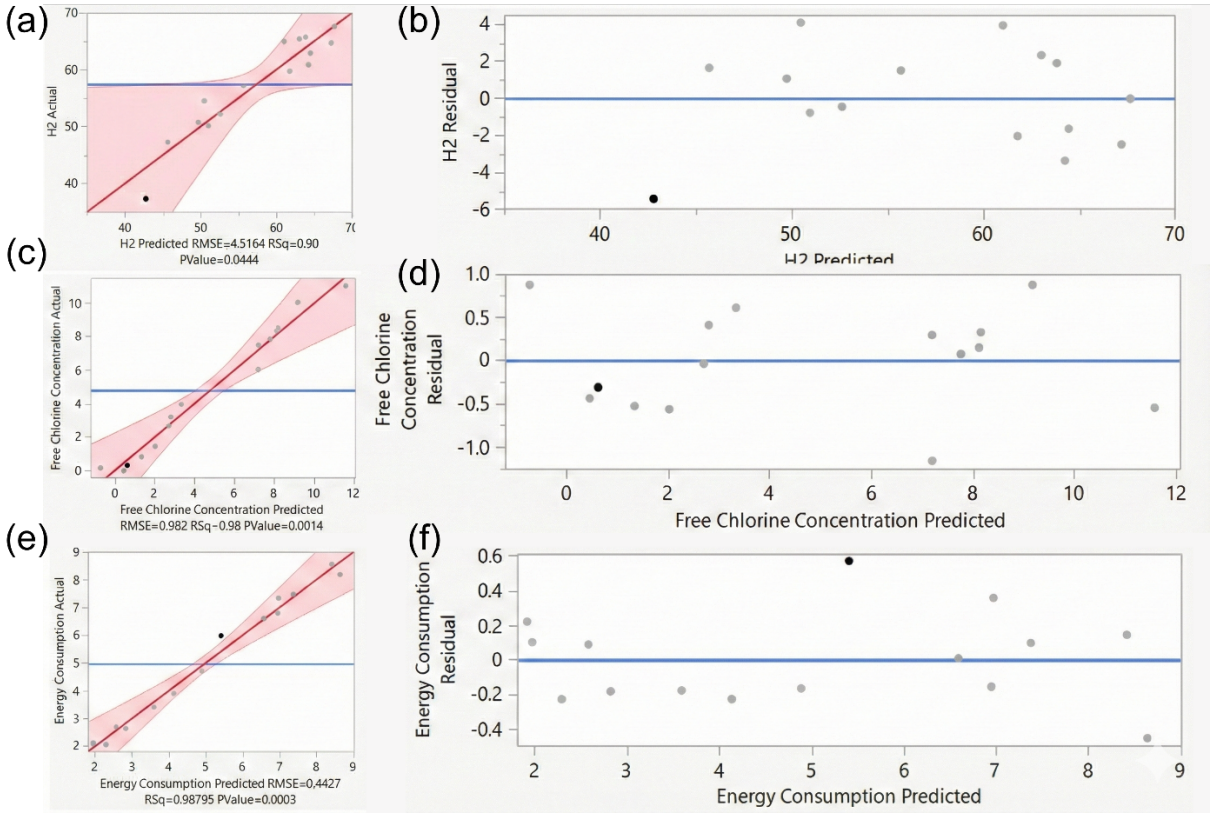

227

228 **Figure S7.** Statistical diagnostic plots for the regression models summarized in Table 2. The left

229 column (a, c, e) displays the Actual versus Predicted response values. The right column (b, d, f)

230 displays the Residuals versus Predicted response values. (a, b) Hydrogen Evolution Rate. (c, d)

231 Aqueous Free Chlorine Concentration. (e, f) Energy Consumption.

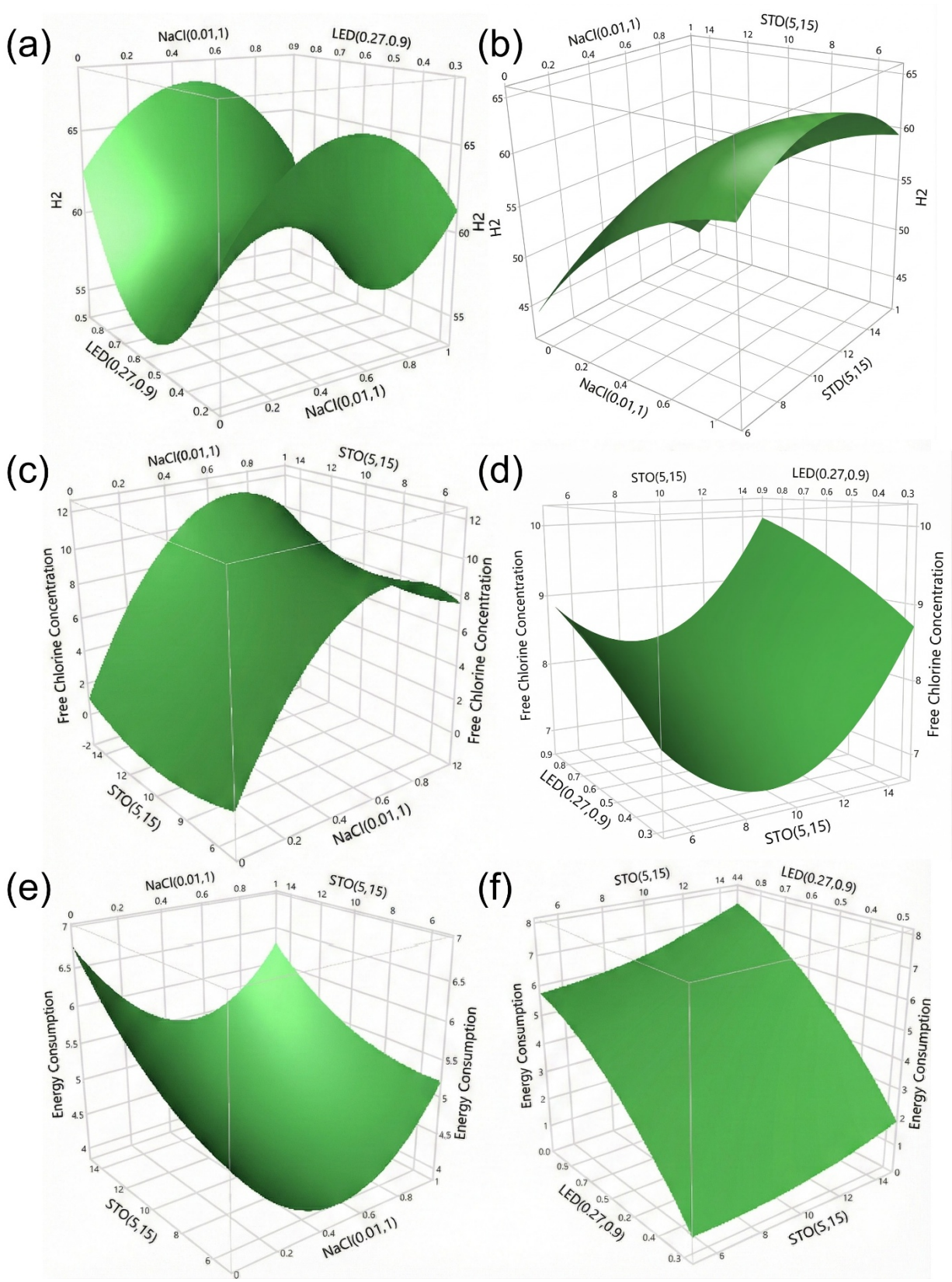
(a)
NaCl(0.01,1)
LED(0.27,0.9)
H2
LED(0,27,0.9)
NaCl(0,01,1)
(b)
NaCl(0.01,1)
STD(5,15)
H2
NaCl(0.01,1)
STD(5,15)
(c)
NaCl(0.01,1)
STO(5,15)
Free Chlorine Concentration
STO(5,15)
NaCl(0.01,1)
(d)
STO(5,15)
LED(0.27,0.9)
Free Chlorine Concentration
LED(0.27,0.9)
STO(5,15)
(e)
NaCl(0.01,1)
STO(5,15)
Energy Consumption
STO(5,15)
NaCl(0.01,1)
(f)
STO(5,15)
LED(0.27,0.9)
Energy Consumption
LED(0.27,0.9)
STO(5,15)

232

Figure S8. Comprehensive set of three-dimensional response surface plots mapping the remaining pairwise interactions in the experimental design space. The vertical axis represents the predicted response variable, while the base axes represent the two interacting experimental factors. (a) Hydrogen Evolution Rate as a function of Salinity (NaCl) and Light Intensity (LED). (b) Hydrogen Evolution Rate as a function of Catalyst Loading (STO) and Light Intensity (LED). (c) Aqueous Free Chlorine Concentration as a function of Catalyst Loading (STO) and Salinity (NaCl). (d) Aqueous Free Chlorine Concentration as a function of Salinity (NaCl) and Light Intensity (LED). (e) Energy Consumption as a function of Catalyst Loading (STO) and Salinity (NaCl). (f) Energy Consumption as a function of Catalyst Loading (STO) and Light Intensity (LED).

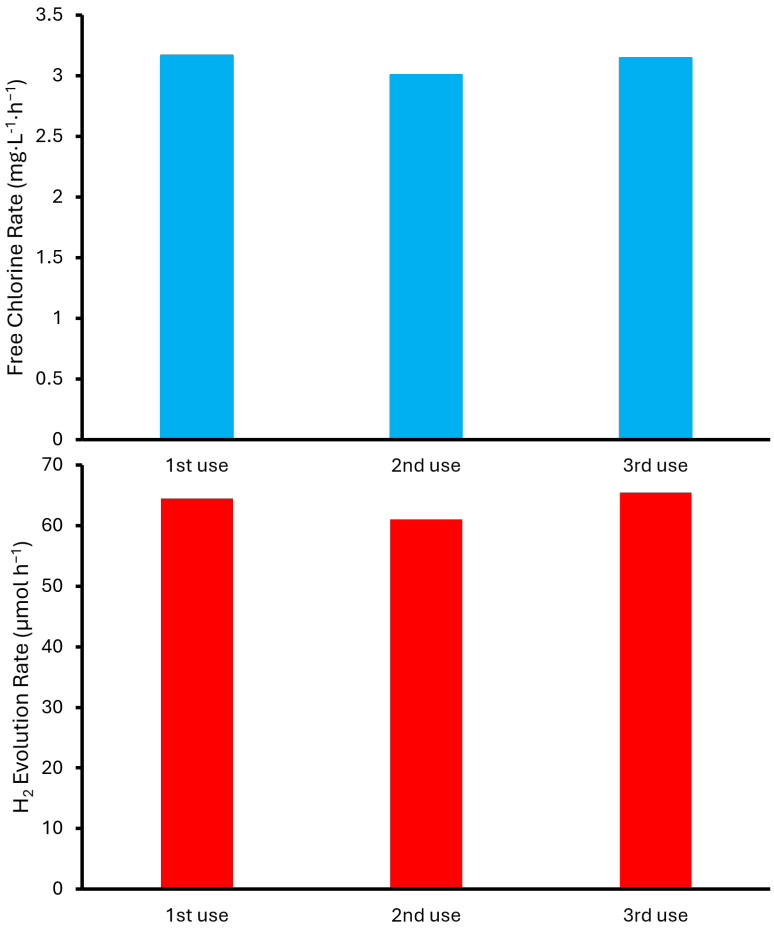

	Cr (ppb)
1st use	3.71
2nd use	2.49
3rd use	2.51

Figure S9. Stability and reusability evaluation of the POF-STO reactor over three consecutive cycles. (a) Free chlorine generation rate and (b) H_2 evolution rate demonstrate sustained catalytic performance. The accompanying table confirms the chemical stability of the cocatalyst by tracking Cr leaching concentrations after each cycle

Reference

(1) Nishiyama, H.; Yamada, T.; Nakabayashi, M.; Maehara, Y.; Yamaguchi, M.; Kuromiya, Y.; Nagatsuma, Y.; Tokudome, H.; Akiyama, S.; Watanabe, T.; et al. Photocatalytic solar hydrogen production from water on a 100-m2 scale. *Nature* **2021**, *598* (7880), 304-307. DOI: 10.1038/s41586-021-03907-3.

(2) Fu, H.; Pan, Z.; Lai, Y.-J. S.; Ananpattarachai, J.; Serpa, M.; Shapiro, N.; Zhao, Z.; Westerhoff, P. Green hydrogen production via a photocatalyst-enabled optical fiber system: A promising route to net-zero emissions. *Energy and Climate Change* **2025**, *6*, 100175. DOI: https://doi.org/10.1016/j.egycc.2025.100175.

(3) Fu, H.; Ryoma, I.; Lai, Y.-J. S.; Ananpattarachai, J.; Serpa, M.; Shapiro, N.; Zhao, Z.; Pan, Z.; Westerhoff, P. Bridging Materials Innovation with an Efficient Photocatalyst-Enabled Optical Fiber Reactor for H2O2 Production. *Environmental Science & Technology* **2025**, *59* (28), 14716-14727. DOI: 10.1021/acs.est.5c04043.
(4) Wang, T.-H.; Lai, Y. S.; Tsai, C.-K.; Fu, H.; Doong, R.-A.; Westerhoff, P.; Rittmann, B. E. Efficient CO2 Conversion through a Novel Dual-Fiber Reactor System. *Environmental Science & Technology* **2024**, *58* (31), 13717-13725. DOI: 10.1021/acs.est.3c10274.
(5) Wong, C. C. Y.; Preso, D. B.; Qin, Y.; Sinhmar, P. S.; Zong, Z.; Kwan, J. Ultrasound-driven seawater splitting catalysed by TiO2 for hydrogen production. *International Journal of Hydrogen Energy* **2025**, *111*, 723-734. DOI: https://doi.org/10.1016/j.ijhydene.2025.02.327.
(6) Jiang, Y.; Qi, Z.; Yang, W.; Zhang, Y.; Feng, X.; Yang, P.; Qin, P.; Huang, F. Ir/TiO2 Heterojunctions with in Situ Defects and Surface Plasmon Resonance: Chloride-Resistant Catalyst for the Photocatalytic Hydrogen Evolution from Seawater. *Angewandte Chemie International Edition* **2026**, *65* (3), e19008. DOI: https://doi.org/10.1002/anie.202519008 (acccessed 2026/04/10).
(7) Adnan, R. H.; Ng, Y. H. Clean production of chlorine (Cl2) and hypochlorous acid (HOCl) from photocatalytic and photoelectrochemical seawater splitting. *Materials Horizons* **2026**, 10.1039/D5MH01556A. DOI: 10.1039/D5MH01556A.
(8) Xiao, S.-T.; Wu, S.-M.; Wu, L.; Dong, Y.; Liu, J.-W.; Wang, L.-Y.; Chen, X.-Y.; Wang, Y.-T.; Tian, G.; Chang, G.-G.; et al. Confined Heterojunction in Hollow-Structured TiO2 and Its Directed Effect in Photodriven Seawater Splitting. *ACS Nano* **2023**, *17* (18), 18217-18226. DOI: 10.1021/acsnano.3c05174.
(9) Okada, T.; Kodera, M.; Miseki, Y.; Kusama, H.; Gunji, T.; Sayama, K. Simultaneous production of hydrogen and chlorine through overall brine splitting with a particulate photocatalyst. *Chemical Communications* **2024**, *60* (24), 3299-3302, 10.1039/D4CC00136B. DOI: 10.1039/D4CC00136B.
(10) Shi, Y.; Shou, H.; Li, H.; Zhan, G.; Liu, X.; Yang, Z.; Mao, C.; Cheng, J.; Zhang, X.; Jiang, Y.; et al. Visible Light-Driven Conversion of Carbon-Sequestrated Seawater into Stoichiometric CO and HClO with Nitrogen-Doped BiOCl Atomic Layers. *Angewandte Chemie International Edition* **2023**, *62* (24), e202302286. DOI: https://doi.org/10.1002/anie.202302286 (acccessed 2026/04/10).